A Brief Literature Survey of Compton and Hybrid Imaging Technologies for Medical Imaging

Joseph Cilento

A Master's Report Submitted to the Faculty of the

COLLEGE OF OPTICAL SCIENCES

In Partial Fulfillment of the Requirements

For the Degree of

MASTERS OF SCIENCE

In the Graduate College

2023

Table of Contents

Abstract

In the grand scheme of medical imaging techniques, Compton imaging is a relatively recent endeavor. Hybrid techniques that involve Compton imaging are even more novel, with research and development being performed currently to create medical imaging devices that incorporate Compton along with other imaging techniques such as PET or Coded Apertures. The reason Compton imaging is relatively difficult to implement is that it deals with higher energy photons, between 1 keV and 1 MeV. At these energies, standard photoelectric and photon-counting detectors have difficulties recording data accurately, and resolution and dynamic range suffer. Detector techniques such as a scattering ring as well as Coded Aperture masks, in addition to specific Compton reconstruction algorithms, allow photons with these higher energies to be observed similarly to standard means. Compton imaging is difficult to implement for the same reason why it is so attractive in the medical imaging field. Promising isotopes used in Targeted Alpha-Particle Therapy (TAT) such as ^{225}Ac and ^{89}Zr decay in such a way that they emit radiation at these higher energies. Having imaging technology that can natively detect where these isotopes are in the body is a large step forward in terms of both treatment and imaging methods. By experimenting with different methods of Compton and hybrid imaging with small animal imaging, we can learn what the advantages and drawbacks are for these techniques and amend them as necessary to make them fit for humans.

1 Introduction

In the grand scheme of medical imaging techniques, Compton imaging is a relatively recent endeavor. Hybrid techniques that involve Compton imaging are even more novel, with research and development being performed currently to create medical imaging devices that incorporate Compton along with other imaging techniques such as PET or Coded Apertures. The reason Compton imaging is relatively difficult to implement is that it deals with higher energy photons, between 1 keV and 1 MeV. At these energies, standard photoelectric and photon-counting detectors have difficulties recording data accurately, and resolution and dynamic range suffer. Detector techniques such as a scattering ring as well as Coded Aperture masks, in addition to specific Compton reconstruction algorithms, allow photons with these

higher energies to be observed similarly to standard means. Compton imaging is difficult to implement for the same reason why it is so attractive in the medical imaging field.

Before delving into the current research and applications of Compton and hybrid imaging techniques, it is important to discuss the ways light interacts with matter at certain energies and provide a brief overview of medical imaging techniques. It will be shown that some techniques lend themselves to be used in hybrid imaging better than others due to the nature of the Compton effect and how they acquire their data.

1.1 Light and its Interaction with Matter

Depending on the energy of a photon, light can behave in three general ways when interacting with matter. The first of which is called the "Photoelectric Effect," and it can occur at photon energies as low as 2 eV, and as large as 100 keV. This phenomenon involves a photon incident on a metal or semiconductor, and if certain parameters are met, the photon causes an electron to dislodge from the material. At lower energies an electron is dislodged from the valence shell, and at higher energies an electron is dislodged from an inner shell. One of the most important parameters in determining whether an electron will be emitted from the material is the type of metal/semiconductor and the frequency of the incoming photon [1]. Contrary to intuition, the intensity of the incident light does not play a large role in the emission of electrons, but it is instrumental in determining the amount of emitted photocurrent. Each material has its own "work function" or minimum energy required to dislodge an electron. Since the energy of a photon is only dependent on its frequency, it can be interpreted that each material has a cutoff frequency such that a photon must have at least that frequency in order to cause the photoelectric effect. Once the threshold is reached, the kinetic energy of the emitted electrons becomes larger as the energy of the photon increases.

Detectors that operate on the premise of the photoelectric effect want to generate a photocurrent when exposed to light, so alkaline metals are typically used when crafting detectors since they have low work function. Semiconductors are used in detector circuits as they are composed of p-type and n-type materials. The incident photons excite the electrons on the p-type material which then move toward the n-type material inducing a measurable photocurrent. Figure 1 shows a circuit demonstrating the photoelectric effect. Having a detector made of a material with a higher work function would restrict the wavelengths of

light accepted and also limits the photocurrent. Imaging methods such as PET and SPECT operate on the photoelectric effect.

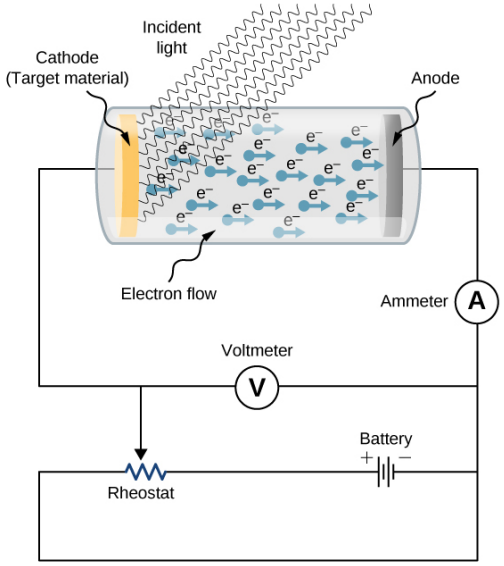

Figure 1: Representation of how the photoelectric effect generates a photocurrent [1]. Using the ammeter, voltmeter, and rheostat the photocurrent and potential difference can be measured.

At higher energies typically between 0.1 and 1 MeV, which are the energies of x-rays and low-energy gamma rays, the "Compton Effect" can be observed. Instead of being absorbed into a material completely and imparting all of its energy into an electron, a photon (mostly thought of as a particle in this context) hits an electron, imparting some of its energy onto the electron, and scattering onward with less energy. This abides by the law of conservation of momentum and energy according to special relativity. Depending on the energy of the incident photon Compton scattering can be observed by firing a gamma ray at a material. The photon is then scattered by the first material, then subsequently absorbed by the second, inducing a current. High-power photons can pass through (and be attenuated by) a solid object, and then be imaged by a Compton scattering detector. This situation could not occur with low-energy photons. Figure 2 shows an x-ray undergoing Compton Scattering.

During a Compton event, the scattering angle of the photon is dependent on its energy at the moment it interacts with a material. When it comes to making Compton detectors, it is imperative that the detector has some field of view. As will be seen later, some Compton and hybrid imaging techniques have a ring of detectors. Compton imaging is desirable not only for imaging high-energy radiation, but it can also be used to reconstruct the 3D spatial

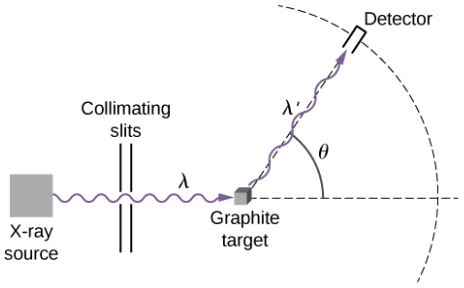

Figure 2: Diagram of the Compton effect from an x-ray source [1]. After the collision, the photon is scattered at an angle θ and has less energy, resulting in a larger wavelength λ'.

coordinates of these interactions [2]. Compton imaging has been around since the 1960's, originally used in astronomy. Recently, teams have been exploiting the Compton effect in the medical realm. Certain isotopes that are proving effective in cancer treatment decay with high radiation, usually unseen by medical imaging techniques such as PET and SPECT. With the development of these Compton medical imaging techniques, cancer treatment and observation can both grow together.

In order to derive the Compton scattering equation, the laws of conservation of momentum and energy, as well as the relativistic definitions of momentum for photons must be recalled [1]. Since the elements involved in Compton scattering are traveling at (or close) to the speed of light, their quantities such as energies and momentums must be treated relativistically. Thus, the total energy of the objects involved cannot be the simple addition of potential and kinetic energies as is standard in classical calculations. Einstein's famous equation tells us that the rest energy of an object is $E_{rest} = m_{rest}c^2$ where m_{rest} is the rest mass of the object and c is the speed of light. The total relativistic energy of an object is given by

$$E = \frac{m_{rest}c^2}{\sqrt{1-\gamma^2}}, \tag{1}$$

where γ is the ratio of the object's speed to the speed of light, c, $\gamma = v/c$. Subsequently, the magnitude of the relativistic momentum of an object is given by

$$p = \frac{m_{rest}v}{\sqrt{1-\gamma^2}}. \tag{2}$$

Squaring Equation 1 yields

$$E^2 = \frac{m_{rest}^2 c^4}{1 - (v/c)^2}. \tag{3}$$

Since $v^2 - v^2 = 0$, inserting it into Equation 3 leaves it mathematically identical, yielding

$$E^2 = \frac{m_{rest}^2 c^2 (v^2 - v^2 + c^2)}{1 - (v/c)^2}. \tag{4}$$

After distribution and algebraic manipulation, the equation becomes

$$E^2 = \frac{m_{rest}^2 c^2 v^2}{1 - (v/c)^2} + \frac{m_{rest}^2 c^4 - m_{rest}^2 v^2 c^2}{1 - (v/c)^2}. \tag{5}$$

Further manipulation yields

$$E^2 = \left(\frac{m_{rest}^2 v^2}{1 - (v/c)^2} \right) c^2 + m_{rest}^2 c^2 \frac{c^2 - v^2}{1 - (v/c)^2}, \tag{6}$$

which then becomes

$$E^2 = \left(\frac{m_{rest}^2 v^2}{1 - (v/c)^2} \right) c^2 + m_{rest}^2 c^4. \tag{7}$$

Substituting in the definitions for rest energy and relativistic momentum from Equation 2 into Equation 7 yields

$$E^2 = p^2 c^2 + E_{rest}^2. \tag{8}$$

Thus, the total relativistic energy is the square root of the sum of the squares of the rest energy and the "relativistic kinetic energy", pc. For photons, which have no mass, their relativistic momentum is represented by

$$p = \frac{E}{c} = \frac{h\nu}{c} = \frac{h}{\lambda}, \tag{9}$$

where ν is the frequency of the photon, h is Planck's constant, and λ is the wavelength of light. For the Compton scattering event, invoking conservation of momentum yields

$$\vec{p}_0 = \vec{p}_1 + \vec{p}_e, \tag{10}$$

where $\vec{p}_0$ is the momentum of the incident photon, $\vec{p}_1$ is the momentum of the photon after scattering, and $\vec{p}_e$ is the momentum of the electron after scattering. It is important to define

these as vector quantities, as directional momentum is also conserved. If Equation 10 is manipulated to have the photon momentums on one side and then the equation is squared, it yields

$$p_e^2 = p_0^2 + p_1^2 - 2\vec{p_0} \cdot \vec{p_1}. \tag{11}$$

Recalling the definition of the dot product yields

$$p_e^2 = p_0^2 + p_1^2 - 2p_0 p_1 \cos(\theta), \tag{12}$$

where θ is the scattering angle of the photon, relative to its incident direction. At rest, the energy of the electron is given by $E_{e_{rest}} = m_e c^2$, where m_e is the mass of an electron. After the collision, the total energy of the electron becomes $E_e = \sqrt{E_{e_{rest}}^2 + p_e^2 c^2}$. Now conservation of energy implies

$$p_0 c + E_{e_{rest}} = p_1 c + \sqrt{E_{e_{rest}}^2 + p_e^2 c^2}. \tag{13}$$

After manipulating and squaring Equation 13, it becomes

$$E_{e_{rest}}^2 + c^2(p_0 - p_1)^2 + 2cE_{e_{rest}}(p_0 - p_1) = E_{e_{rest}}^2 + p_e^2 c^2, \tag{14}$$

which then can be further manipulated to become

$$p_e^2 = p_0^2 + p_1^2 - 2p_0 p_1 + \frac{2}{c} E_{e_{rest}}(p_0 - p_1). \tag{15}$$

Using the definition for p_e^2 found in Equation 15 and substituting it into Equation 12 yields

$$\frac{E_{rest}}{c}(p_0 - p_1) = p_0 p_1 (1 - \cos(\theta)). \tag{16}$$

By substituting in the definitions of E_{rest} and the momentum of a photon from Equation 9, the Compton Scattering equation is

$$\cos(\theta) = 1 + m_e c^2 \left(\frac{1}{E_1} - \frac{1}{E_0} \right) = 1 + \frac{m_e c^2}{h}(\lambda_0 - \lambda_1). \tag{17}$$

Since detectors can determine the energy of a photon much easier than its wavelength, the energy definition of Equation 17 is used in image reconstruction. Usually, E_0 is a known

quantity given a certain radionuclide and E_1 is a measured energy from an absorption detector, so the uncertainty of the scattering angle θ is given by

$$\Delta\theta = \frac{m_e c^2}{E_1^2\sqrt{1-(1+m_e c^2(\frac{1}{E_1}-\frac{1}{E_0}))^2}}\Delta E_1, \tag{18}$$

which can be found by standard uncertainty calculations, where the only other uncertainty is E_1. Now, consider a situation in which the energy of the Compton interaction E_s is measured using a scattering detector, rather than measuring the energy of the outgoing photon with an absorption detector. E_s can be thought of as the energy added to the scattering detector from the incident gamma ray during the Compton event, and the difference in the energy of electron before and after scattering. E_0, E_1, and E_s can be related by $E_0 = E_s + E_1$. Thus, if E_0 is known and E_s is measured, the angle of scatter can be found using

$$\cos(\theta) = 1 - m_e c^2 \frac{E_s}{E_0(E_0 - E_s)}. \tag{19}$$

Since E_0 is still a known quantity, the uncertainty in the angle θ is given by

$$\Delta\theta = \frac{m_e c^2}{(E_0 - E_s)^2}\left(-\frac{m_e c^2 E_s(m_e c^2 E_s + 2E_0E_s - 2E_0^2)}{E_0^2(E_0-E_s)^2}\right)^{-1/2}\Delta E_s. \tag{20}$$

Although the projects in this paper use known values for E_0 based on a given nuclide, there exists a situation in which the incident gamma ray energy is unknown, and the scattering angle is inferred from the energies measured by the scattering and absorption detectors. If that is the case, then the scattering angle can be found using

$$\cos(\theta) = 1 - m_e c^2 \frac{E_s}{E_1(E_s + E_1)}, \tag{21}$$

where E_s is measured with the scattering detector and E_1 is measured with the absorption detector post-scatter. Since neither E_s nor E_1 are known quantities, they each have uncertainties associated with their measurement. Thus the uncertainty in scatter angle becomes

$$\begin{aligned}(\Delta\theta)^2 = &\left(\frac{m_e c^2}{(E_1+E_s)^2}\left(\frac{m_e c^2 E_s(2E_1^2 + 2E_1E_s - m_e c^2 E_s)}{E_1^2(E_1+E_s)^2}\right)^{-1/2}\Delta E_s\right)^2 \\ &+\left(\frac{m_e c^2 E_s(E_s+2E_1)}{E_1^2(E_1+E_s)^2}\left(\frac{m_e c^2 E_s(2E_1(E_1+E_s) - m_e c^2 E_s}{E_1^2(E_1+E_s)^2}\right)^{-1/2}\Delta E_1\right)^2.\end{aligned} \tag{22}$$

Considering the complexity in the error calculation of Equation 22, it is understood why teams use isotopes in which the incident gamma ray energy is known. Further manipulation and interpretation of the Compton Scattering equation for the purposes of image reconstruction will be discussed further in this paper.

Lastly, at energies above 1.022 MeV light can undergo "Pair Production." When a high-energy photon gets near an atom, it can decay into a particle and an anti-particle, typically an electron and a positron. The energy threshold for pair production is 1.022 MeV since the rest mass of an electron (and positron) is 0.511 MeV. The positron subsequently annihilates producing two annihilation photons that undergo subsequent Compton scattering or photoelectric absorption in the material. One (single escape) or both (double escape) of these annihilation photons may escape the detector volume [3]. A diagram of pair production is shown in Figure 3. Unlike other optical events involving detectors, pair production is not a Poisson random event, as the process is dependent on photon energy and material properties, among other parameters. Gamma ray detectors do exist that can handle photons experiencing pair production, but they are usually in the fields of astronomy, high-energy physics, mineralogy, nondestructive evaluation, and non-proliferation. However, they are beyond the scope of this paper.

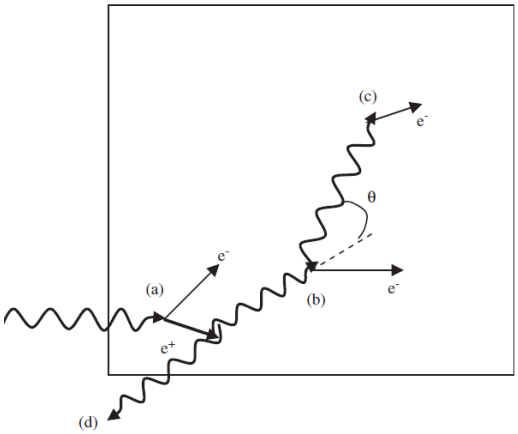

Figure 3: Representation of pair production in psuedo 3D space [3]. Firstly, an incident photon at energy above 1.022 MeV annihilates at (a) producing an electron and a positron. The positron then subsequently annihilates and one of the photons undergoes Compton scattering at (b). After the Compton scattering event, the reduced-energy photon undergoes photoelectric absorption at (c), kicking out an electron into the detector. (d) shows a single escape scenario, in which one of the photons from the positron annihilation escapes the detector.

1.2 Established Medical Imaging Techniques

With technological advancements and greater understandings of the properties of light and sound, many types of medical imaging have been developed. Some methods lend themselves better to be used in hybrid imaging systems with Compton detectors, but imaging using multiple methods allows for a better understanding of the specimen being imaged. This section discusses some of the popular medical imaging techniques.

Ultrasound is a relatively cost-effective imaging technique that takes advantage of sound waves and acoustics of tissues in the specimen. It is a portable technology that can provide instantaneous imaging and has a competitive resolution on the order of 50 ¯m [4]. However, it is limited by the depth of tissue that it can scan through as well as artifacts caused by bone or air. While it has its purposes in medical imaging, ultrasound does not lend itself to hybrid imaging with Compton techniques.

X-ray Computed Tomography (CT) is a popular medical imaging technique. It is highlighted by its resolution on the order of 50 microns, as well as its high contrast between soft tissue and bone [4]. Image contrast can be further improved with iodinated contrast agents as well. Compared to other imaging techniques, CT offers relatively fast imaging times. Despite the positives CT imaging has to offer, the imaging technique has difficulties contrasting tumors from soft tissue, especially if the tumor does not protrude from the tissue. CT also has difficulties imaging high-energy radiation scattering from the specimen. Although not directly used with Compton imaging in hybrid techniques, it will be shown that CT imaging is used in conjunction with hybrid techniques to show a detailed image of the specimen, with the Compton image overlayed.

Single Photon Emission Computed Tomography (SPECT) involves injecting a radiolabeled nuclide that is subsequently imaged by a gamma camera [4]. The nuclide is chosen such that it decays and emits in the low-energy gamma, and it matches with the camera to improve the counting rate and resolution. In some SPECT systems, the camera rotates around the specimen on multiple axes in order to get an entire set of tomographic projections. The spatial resolution of SPECT systems is not quite as precise as CT; it is on the order of 1 mm pre-clinical and 10 mm clinical. With pinhole collimators, parallel hole collimators, or coded aperture masks along with advancements in detector technology and

radiopharmaceuticals, the resolution is improving.

Similar to SPECT, Positron Emission Tomography (PET) involves the use of a radionuclide tracer injected into the body. However, in PET imaging, the nuclide decays into a positron that collides with an electron, subsequently annihilating and producing a gamma ray that can be imaged. The spatial resolution of PET systems is about 1.5 mm pre-clinical, and about 6 mm clinical. PET can also create 3D images like SPECT. What separates PET and SPECT imaging from other imaging techniques such as CT, Ultrasound, and MRI, is that they are used to image biological processes rather than anatomy. "With carefully designed labelled molecular probes, the target can be a specific metabolite, a tumour-specific antigen, or a gene being expressed. The functions being revealed could be a signal transduction in neurological systems, development of tumour under controlled environments, or the mechanism of a gene sequence" [4].

Two major sources of error in PET imaging come from phenomena known as "positron range" and "non-collinearity" [5]. Positron range is when a positron is formed it does not immediately annihilate and can travel for some time, on the order of nanoseconds, before it annihilates into two photons. Although it doesn't immediately seem that positron range would be a significant issue, positrons can travel on the order of a few centimeters, depending on the material they are in [5]. The distance a positron travels from the decay that creates it is a limiting factor in the design of high-resolution scanners and studies using them. As shown in Figure 4, a positron has a possibility of traveling significantly far before annihilation, causing blur on the detector.

Another consequence of positron range is non-collinearity, in which positronium annihilates with a non-zero net momentum, causing the subsequent photons to emit at an angle smaller than 180°. This is another limiting factor when it comes to minimizing blur for PET systems, as there is no way to tell when non-collinearity occurs from just detected signals. After Monte Carlo simulations testing non-collinearity effects, the angle of deviation from emitted photons was centered at 180° and had a standard deviation of 0.5° [5]. As shown in Figure 5, the non-collinearity phenomenon is Gaussian in nature. With the distributions of these effects being mostly known, image reconstruction algorithms may be able to compensate for photon range and non-collinearity. However, since they are still random events, there still exists a fundamental limit to the spatial resolution of PET systems.

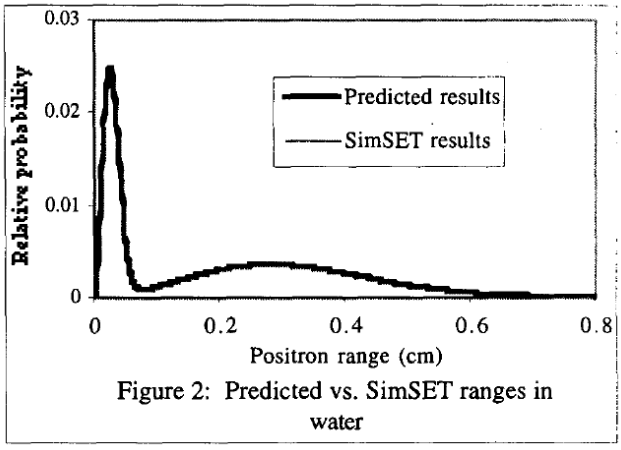

Figure 4: Predicted positron range of a hypothetical positron emitter in water [5]. This plot represents the probability of traveling a radial distance from the point of origin, integrated over all angles. Due to the Jacobian of spherical integration, the probability seems to go to 0 at 0 cm. However, the positron annihilating without traveling is the most likely outcome.

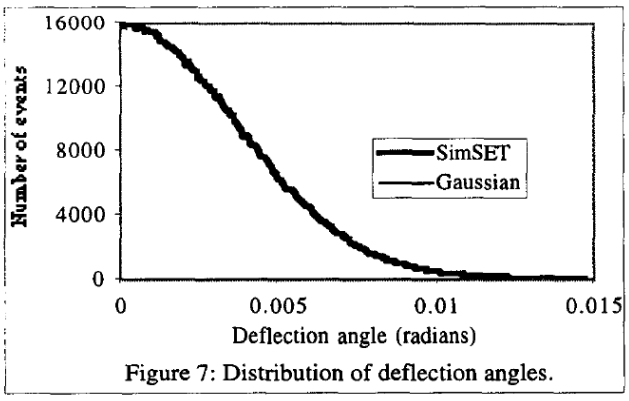

Figure 5: Non-Collinearity distribution [5]. Depending on the geometry of the detector, non-collinearity effects can contribute on the order of a centimeter of blurring.

Both PET and SPECT operate on similar principles when it comes to imaging; both rely upon a radionuclide decaying in the specimen, the tissue in the specimen then attenuating the radiation, and the signal being collimated and read by a detector. PET can be thought of as collimating electric charges whereas SPECT can be thought of as collimating photons. Both methods typically take advantage of a scintillation detector (a crystal that can produce a burst of photons when hit with gamma rays) that feeds to a photomultiplier tube that increases the gain of the signal, making it readable. These methods are usually limited by collimator blur, the sensitivity of the detector, as well as scattering from the body of the specimen. PET systems typically have higher resolutions and sensitivities than SPECT systems but come with the drawback that they can only image positron emitters.

PET and SPECT techniques play nicely with Compton techniques, as they produce high-

energy radiation that can undergo Compton events. As will be discussed later, the choice of the radionuclide tracer will not only target and treat cancerous/anomalous parts of the specimen but will also allow for a better image using hybrid techniques.

1.3 Detection and Gain Involving Low Photon Counts

Since PET and SPECT techniques rely on radionuclides decaying and subsequently producing measurable photons, it is important to discuss low photon number or single photon detection methods. The most long-established photon-counting technology is the photomultiplier tube (PMT), developed in 1949 [6]. A basic PMT consists of a vacuum tube with a photocathode for light absorption, from which electrons are liberated through the photoelectric effect. This photocurrent is then multiplied by a cascade of secondary electron emissions from dynodes of increasing voltage (up to 10 kV) producing a macroscopic current pulse of over 10^6 electrons, which can be read as a current. PMTs have a quantum efficiency on the order of 25-40% which is certainly manageable depending on the system.

Another method used to increase gain with single-photon detection systems is an Avalanche Photodiode. Avalanche photodiodes are solid-state alternatives to PMTs and can have a long wavelength cutoff as a result of the Silicon bandgap. They take advantage of p-n or p-i-n junctions described in the photoelectric effect portion in Section 1.1. A typical Silicon Avalanche photodiode has a diameter of approximately 180 microns, a peak wavelength of 650 nm, and a quantum efficiency of around 65% Avalanche photodiodes have a lower operating voltage compared to PMTs, typically around 400 V. Newer generation Si Avalanche photodiodes are about 50 microns in diameter, require less voltage to operate, but have a tradeoff in that its peak wavelength becomes 550nm and its quantum efficiency drops to 49% [6]. In order to work at higher wavelengths, the materials are typically changed to Ge and InGaAs and are used mostly for telecommunication. As seen in Figure 6, different Avalanche photodiode structures can be altered to optimize for certain situations. Unlike PMTs, Avalanche photodiodes do not have known "gain stages" since there is only one bias across the entire system. Because of this, they have larger gain variations than PMTs and are more random.

Since these gain methods are based on the photoelectric effect, a lower energy (larger wavelength) photon would not be as easily read by PMTs and Avalanche photodiodes.

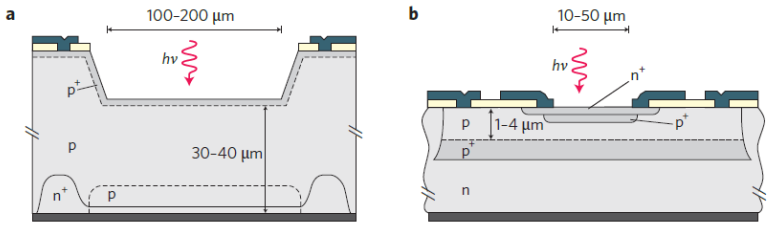

Figure 6: Two typical structures for Avalanche photodiodes [6]. a) shows a Thick-junction detector that has a device structure optimized for high detection efficiency and low dark counts, while b) shows a Shallow-junction planar that is optimized for a device structure optimized for low-timing jitter requiring low bias voltages.

Frequency-Up conversion is a method that lowers the wavelength of incident photons such that they can be better read by single-photon detectors. A weak signal of low frequency is combined with a strong pump of large frequency and their output is the sum of the two. Increasing the frequency of light shortens its wavelength. In periodically poled lithium niobate, using a pump signal at 1064 nm allows 1550 nm photons to be converted to 630 nm photons with 90% efficiency. Drawbacks of frequency-up conversion include the difficulty of stabilizing the nonlinear crystal, the presence of nonlinear processes that lead to fluorescence at the up-conversion wavelength resulting in high background count rates, and high input and output coupling losses for waveguides. A diagram of frequency-up conversion is shown in Figure 7. In the current state of Compton and hybrid imaging methods, they use high-energy photons since it is required to undergo Compton scattering, frequency-up conversion is not typically required but it is still worth mentioning as it may become useful as the development of radioisotopes and detectors moves forward.

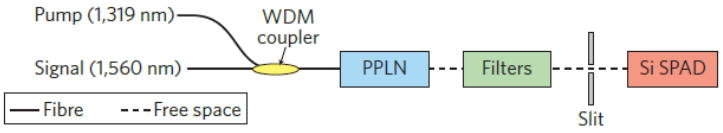

Figure 7: A Frequency-up Conversion detector in which a 1560 nm wavelength photon is converted to a 715 nm wavelength photon [6].

1.4 Coded Aperture Masks

Coded aperture masks are used in gamma ray imaging techniques and use multiple apertures in a manner analogous to pinhole imaging, together with image reconstruction techniques

to decode the overlapping images from many apertures. "The design demonstrated in this paper utilizes a thin pixelated silicon spectrometer, a coded aperture mask, and a monolithic full-energy NaI(Tl) scintillation detector behind the coded aperture. This configuration provides the same angular resolution and wide field-of-view as a conventional Compton camera with the same geometry, without requiring a second pixelated detector. This also results in considerable simplification of the data acquisition and data processing systems. The principal advantage of the configuration presented here is that thick, monolithic, full-energy spectrometers (e.g. NaI, CsI, LaBr) can be used to provide detection efficiencies, up to 1500 keV, that exceed 90% with peak-to-total ratios of $\geq$70% and are available in standard configurations with cylindrical dimensions up to 10 inches in diameter and length. No pixelated spectrometer with such efficiencies is commercially available" [7]. By covering a high-energy detector with a coded aperture, it casts a "shadow" onto the detection plane, and the geometry and type of mask can be made to act as a collimator which can optimize reconstruction but at the cost of efficiency.

Since scattered Compton rays scatter uniformly in angle, measuring the incident ray energy can also determine its angle of scatter. For the particular coded aperture shown in Figure 8, a single monolithic Compton layer is supplemented by a coded aperture as a detection layer rather than a pixelated layer. These two layers are used to determine photon position and energy without sacrificing resolution. "Thus the coded aperture system provides the needed estimate of the scattered photon flux in each direction that falls within the square aperture of the mask" [7]. If half of the mask is left open the count rate is maximized but comes with the cost of path ambiguity and increased noise levels. Another concern that is present with coded aperture masks is that a high-energy photon might undergo pair production when it gets near the mask or detector. Monte Carlo simulations showed that photons with energies as high as 1.5 MeV (much higher than the 1.022 MeV threshold) experience pair production less than one-third of one percent of the time.

One of the strengths of using coded aperture masks is the detection of point sources. "The simulation of point sources has demonstrated the potential of the system to correctly identify isotropic sources, and locate their correct position within an angular area of $7.5^\circ \times 7.5^\circ$. Sources with activities of a few mCi are easily imaged from distances up to 10 m. The source strengths used here appear to exceed by far the detection limit, but that limit cannot

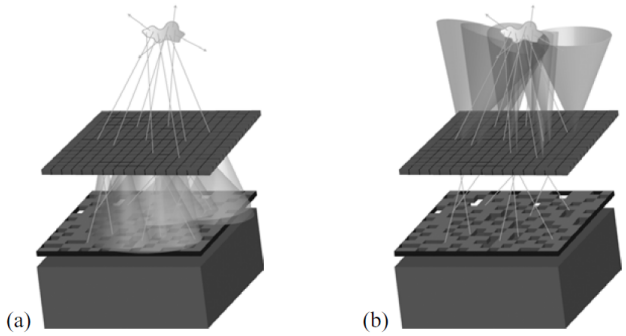

Figure 8: Coded Aperture showing a forward and adjoint transfer of light in (a) and (b), respectively [7]. When radiation is incident on the mask, it acts almost like a pinhole.

be properly determined until an actualization of the system is built and tested. The system appears to have the ability to perform useful radiological scanning during decontamination and decommissioning and other types of survey" [7]. Although the coded aperture imaging system was idealized in the simulations, the results of both image reconstruction as well as point-source detections were promising. The results of image reconstruction are shown in Figure 9, and although it seems that the Maximum Likelihood Estimate (MLEM) of the coded aperture Compton camera are significantly worse than the Compton camera without the coded aperture, note the counts for each situation. Some recent developments of hybrid imaging systems that will be discussed further do take advantage of coded apertures in order to optimize their system.

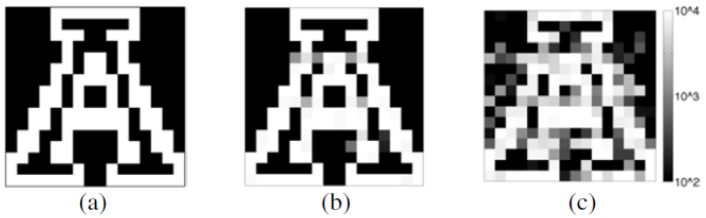

Figure 9: (a) Input object ($N_i = 1.06 \cdot 10^6$)
(b) MLEM of the Compton camera ($N_i = 235099$)
(c) MLEM of the coded aperture Compton camera ($N_i = 117891$) [7].
Here, the count refers to the count rate of how many photons from the object reached the detector in the simulation.

2 Compton and Hybrid Medical Imaging

Although Compton imaging techniques have been used in fields such as astronomy, it is a relatively new development for medical imaging. In the literature review for this report, one

of the earliest papers on combining Compton imaging with other medical imaging methods was in 2007. Unfortunately, that paper did not have a working prototype and only involved simulations. The bulk of papers on the topic were published extremely recently, between 2020 and 2022. Luckily, the more recent papers did have prototypes that were tested, imaging multiple types of radionuclides, as well as implementing different types of data acquisition and reconstruction techniques. This section will discuss hybrid imaging systems, highlighting their development, as well as their methods of image capture and reconstruction.

2.1 Early Simulations and Methods of Hybrid Imaging

One of the earlier discussions of using Compton techniques in conjunction with PET methods for the purposes of medical imaging involves β^+ and γ emissions from ^{44}Sc radio-nuclide were measured to trace back its coincidence [8]. The decay of ^{44}Sc produces positrons that can be imaged by conventional PET methods, along with 511 keV gamma rays which can be imaged by a Compton telescope detector. In this situation, liquid Xenon was used as the detector due to its high atomic number, scintillation, and ionization yields. The detection of the β^+ and γ emissions can happen almost simultaneously, leading to a quick reconstruction of the spatial coordinates of the point of interaction. Figure 10 shows how the use of PET and Compton detection can be used to image events.

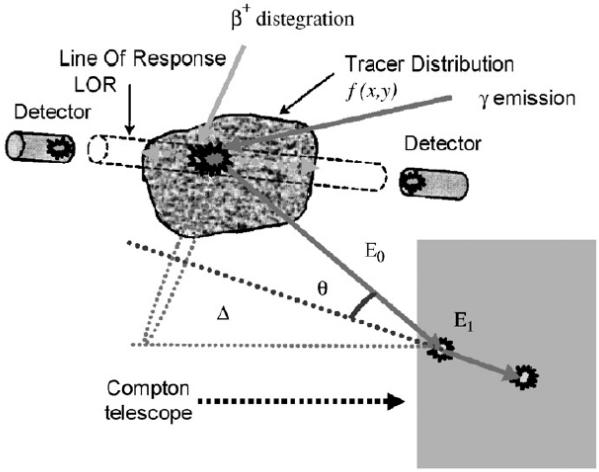

Figure 10: Figure representing how decaying β^+ particles into a body emits a γ ray which can be read by a liquid Xenon Compton telescope [8]. By knowing the energies E_0 and E_1 as well as the line of response, the 3D spatial location of the disintegration can be determined.

With the assumption that the positron and the gamma ray are emitted from the same place in space, the position of the radio-nuclide is then obtained by the intersection of the

direction cone of the gamma ray undergoing Compton scattering along with the reconstructed line of response defined by two 511 keV gamma rays issued from the β^+ annihilation with an electron within the body. Using Equation 19, the angle of the emitted gamma ray is inferred from Compton kinematics, using the measured energy of the scattering detector and the known energy of the incident gamma ray. The scattering angle and the line of response are used to reconstruct the spatial coordinate of the decaay event. For the purposes of imaging, the number of viable $\beta^+\gamma$ emitters is restricted to a select few that emit positrons and gamma rays quasi-simultaneously along with ensuring the energy of the gamma ray is large enough such that the spatial and angular resolutions are not limited. For this prototype, ^{44}Sc was selected for its yield and gamma ray energy, but other isotopes will prove to be useful as well.

A prototype for this system was being developed, with the purpose of testing the camera in a small animal imaging situation. The active volume of the prototype is shown in the left portion of Figure 11. "The implemented geometry consists of a monolithic LXe Compton telescope containing 64 individual cells of 3 by 3 by 12 cm^3 for a total volume of 24 by 24 by 12 cm^3 added as an endcap to an existing micro-PET system (an LSO ring of 26 cm diameter with a field of view of 7.6 cm)" [8]. Although not completed in the paper, the prototype was still tested using Monte Carlo simulations to gauge its accuracy and resolution. As shown in the right portion of Figure 11, the system imaged a point source of ^{44}Sc within a "rat" phantom defined by a water cylinder of 6 cm diameter and 15 cm length.

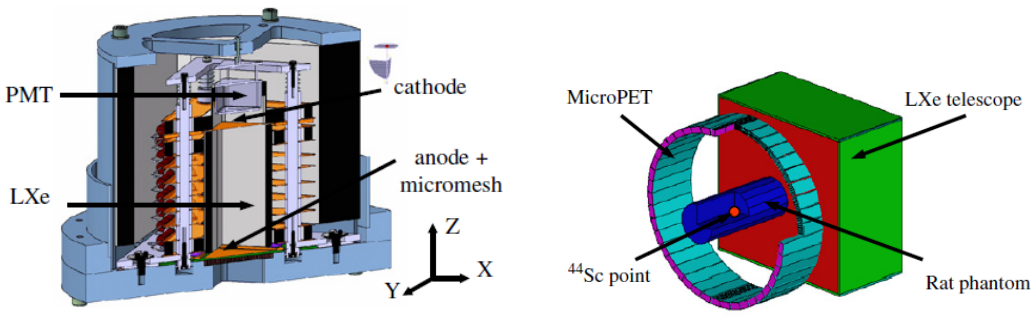

Figure 11: LEFT: Prototype of the liquid Xenon Compton Telescope [8]. Here, the active volume is shown. Notice the PMT used to increase gain.
RIGHT: Liquid Xenon Module associated with a micro-PET system [8]. This system was tested using Monte Carlo simulations. The ring structure shown here will be a hallmark of Compton Hybrid imaging systems.

The results from these simulations showed that the camera system had a potential spatial

resolution of 2.3 mm, which was much better than PET or Compton telescope imaging systems at the time on their own. Although simulations of a hybrid imaging prototype are not as valuable as actual data from a working system, this was an important step towards incorporating Compton imaging into the field of medical imaging.

The team behind the nuclear medical imaging project in 2007 went on to develop the XEMIS1 and XEMIS2 prototypes [9]. The XEMIS prototypes took advantage of triple-gamma imaging, as described earlier, to reconstruct the 3D spatial location of the decay event. A schematic of the XEMIS1 prototype is shown on the left side of Figure 12, and it "consists of a Time Projection Chamber (TPC) of 2.8 cm by 2.8 cm by 12 cm active volume full of liquid xenon. The VUV scintillation photons (178 nm) generated from the gamma ray interactions are detected by a Hamamatsu R7600-06 MOD ASSY photomultiplier tube (PMT) specially designed to work at liquid xenon temperature. The PMT is located at the top of the TPC and it is used as a trigger for the ionization signal acquisition. The charge carriers produced in the ionization are collected by a 64 pixel segmented anode of 2.8 by 2.8 cm^2" [9]. The XEMIS1 prototype saw a spatial resolution along the line of response for a ^{22}Na source of between 100 μm and 10 mm depending on the electric field of the system. It had an energy resolution around 9% (FWHM). These results are impressive considering the difficulties of maintaining a LXe detector. The XEMIS1 prototype set the stage and showed promise for the next development, the XEMIS2. The XEMIS2 system is being developed for small animal imaging and can be seen in the right portion of Figure 12, "the liquid xenon active zone of the detector is a cylinder of 7 cm of inner radius, 19 cm of outer radius. ... Two circular segmented anodes are located at the edges of the active zone. A total amount of 25000 pixels of 3.175 by 3.17 $5mm^2$ size will be present. Around 800 front-end electronics read-out cards of 32 channels each will be used to collect the signals. The active volume will be covered by about 380 Hamamatsu PMTs" [9]. The XEMIS2 has not had a fully realized prototype yet, but simulations show that it has a potential energy sensitivity of 7 % (FWHM) and the precise localization of the emission point along the line of response can be found, within the order of 1 cm (FWHM). The XEMIS2 system reconstructs the image in two phases, first obtaining a raw image from the reconstructed LOR and Compton cone intersections, then that raw image is run through a maximum likelihood estimate iterative algorithm [10].

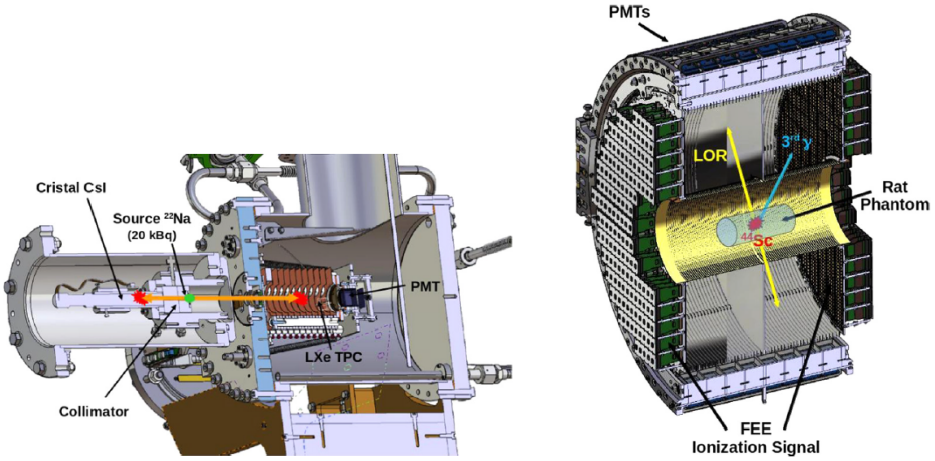

Figure 12: LEFT: Schematic of the XEMIS1 prototype, calibrated with a ^{22}Na source [9]. RIGHT: Schematic of the XEMIS2 prototype [9].

When it comes to in-vivo imaging using Compton methods, the first studies that involved animal specimens in Japan occurred in 2008; prior to that only phantoms were used to approximate the effects of tracers within a living body [11]. Around and before the year 2000, Compton imaging took a long time to produce a satisfactory image, taking on the order of 10+ hours to take enough sufficient measurements in order to adequately reconstruct an image. Improvements in fields such as large-volume crystals, multi-layer configurations, and high-energy resolution scintillators have led to the improved success of in-vivo studies. A gamma ray emission imaging (GREI) system was one of such projects developed in 2001 that used Compton methods to simultaneously measure multiple tracers in-vivo. The GREI system saw significant improvements since then, invoking a second iteration of GREI-II in 2015, which has smaller detectors and improved sensitivity, enhanced front-end processing, and reduced seed-time. Some of the first in-vivo images from produced by the GREI-II are shown in Figure 13.

Although not every team and project will be discussed in detail in this paper, it is worth mentioning a select few systems along with which the materials used for their Compton scatter/absorber and how they evolved in time. Such projects are shown in Table 1. One of the most recent and most interesting projects, "WGI", will be especially discussed further.

2.2 Introduction to Whole Gamma Imaging

In 2020, a team out of Japan was the first to propose a concept called "Whole Gamma Imaging" (WGI) in which PET and Compton imaging could be performed simultaneously,

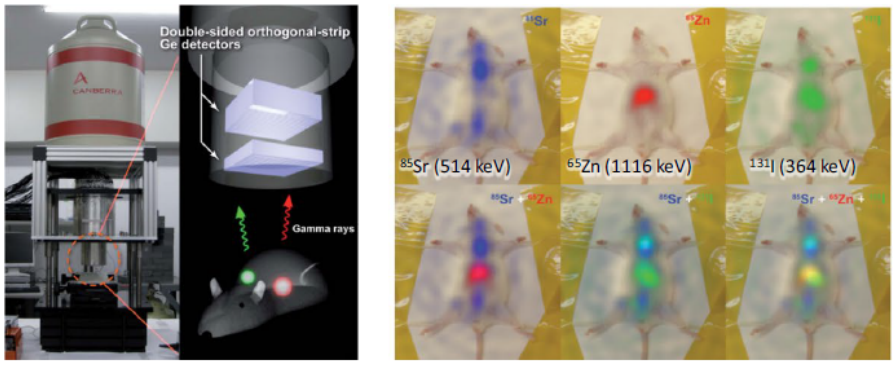

Figure 13: Early method of using Compton methods to simultaneously image multiple tracers in-vivo [11]. (a) shows the GREI and (b) shows its first in-vivo triple tracer imaging results.

Project/Team/Author	Scatterer	Absorber	Year
Singh and Doria	Ge	NaI	1983
Martin et al.	Ge	NaI(Tl)	1993
Bolozdynya et al.	Xe	Xe	1997
C-SPRINT	Si	NaI	1998
RIKEN-GREI	Ge	Ge	2001
Kyoto Univ.	Ar + C_2H_6	NaI(Tl)/$LaBr_3$	2005/2010
JAXA	Si	CdTe	2005
MACACO, MACACO-II	$LaBr_3$	$LaBr_3$	2013/2018
Waseda Univ.	GAGG	GAGG	2017
Polaris J CC	CZT	CZT	2018
QST-Takasaki	GAGG	GAGG	2018
Timepix3 CC	Si	CdTe	2018
The Univ. of Tokyo	GAGG	GAGG	2020
WGI	GAGG	GSO	2020

Table 1: Teams that developed Compton imaging systems along with their detector variations [11].

utilizing all detectable gamma rays from a decaying isotope for imaging. The prototype system involves "an additional detector ring, which is used as the scatterer, is inserted in the field-of-view of a PET ring so that single gamma rays can be detected by the Compton imaging method. In particular, for the non-pure positron emitters which emit an additional gamma ray almost at the same time, triple gamma imaging will be enabled; localization on each line-of-response (LOR) is possible by using the Compton cone of the additional gamma ray" [12]. The WGI system is the first of its kind to implement a ring structure in order to use PET and Compton imaging at the same time, as well as have a working prototype to show it off. Although works published earlier, including the one discussed in Section 2.1, discussed the possibility of simultaneous imaging there were no prototypes developed that

showcased "triple gamma imaging."

Figure 14 shows all possible gamma rays available for imaging from a radioisotope along with which gamma rays are imaged in each mode. Single gamma mode refers to imaging the scattered gamma ray using Compton methods, while triple gamma mode refers to imaging both gamma rays from the positron annihilation in the PET mode as well as the scattered gamma ray in the single gamma mode at once. The most impressive is the triple gamma mode that images all three gamma rays simultaneously using PET and Compton imaging methods.

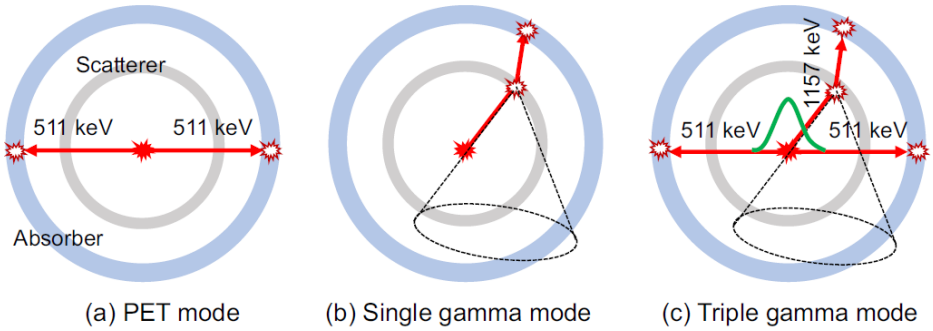

Figure 14: Schematic diagram of how the WGI system will operate in (a) PET mode, (b) Single gamma mode, and (c) Triple gamma mode [12]. Notice the scattering ring (shown in gray) added to the FOV of the PET system.

The beauty of the WGI system is that it can operate in each mode depending on the emitter being imaged. For single gamma ray emitters such as ^{99}Tc and ^{111}In, the system can act like a Compton camera. For positron emitters such as ^{18}F, the system can act like a PET imager, "in the PET mode, a scatterer-scatterer coincidence and a scatterer-absorber coincidence both occur in addition to a typical absorber-absorber coincidence, and the coincidence related to the scatterer may have a potential for better spatial resolution due to the reduced photon acollinearity" [12]. For triple gamma isotopes that emit positrons and gamma rays at nearly the same time such as ^{44}Sc, which was also mentioned in Section 2.1 as a desirable isotope for hybrid imaging, the WGI system can image all the emissions, and can determine the location of the source within a relatively small number of counts.

The actual WGI prototype, which can be seen in Figure 15, uses the ring structure discussed earlier. The specific materials and dimensions for the scatter and absorber parts of the prototype can be seen in Table 2. Something interesting to note is that this team has been working on medical imaging devices for some time and they were able to borrow

ideas and materials from older projects in order to create the WGI prototype, namely, the detector used for the absorber is one of a previous PET imaging prototype system made by them in 2017. Although the prototype in this state was too small to be used for most human imaging, it was also too large for small animal imaging "as spatial resolution in Compton imaging as well as sensitivity largely depend on the source-detector distance, the diameter should be small, e.g. 10 cm, for small animal studies" [12].

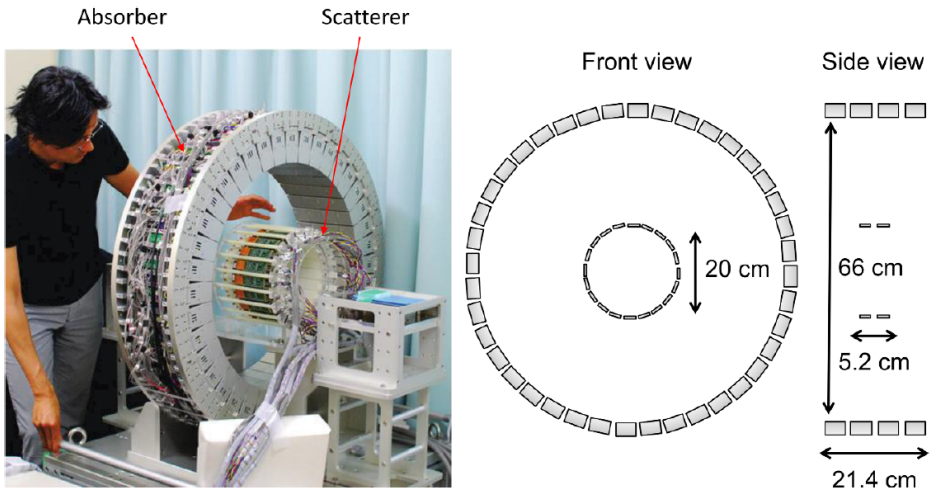

Figure 15: Photo of the WGI prototype along with an illustration of the block detector arrangement [12].

	Scatterer	**Absorber**
Crystal material	GAGG	GSOZ
Crystal array	24 by 24 by 1	16 by 16 by 4
Crystal size	$0.9 \times 0.9 \times 6.0$ mm^3	$2.8 \times 2.8 \times 7.5$ mm^3
Photodetector	64ch TSV-MPPC array (3.2 mm pitch) Hamamatsu S14161-3050HS-08	64ch FP-PMT (6 mm anode pitch) Hamamatsu R10552-100-M64
# of detectors	20 by 2 rings	40 by 4 rings
Ring diameter	20 cm	66 cm
Axial FOV	5.2 cm	21.4 cm

Table 2: Specifications of the WGI prototype [12].

The WGI system uses 3 different image reconstruction methods, for each mode it operates in. In PET mode, it uses the list-mode ordered subset expectation maximization (OSEM) algorithm, which uses the absorber-absorber coincidence and the scatterer-scatterer coincidence to iterate the reconstruction governed by:

$$f_j^{(k,l+1)} = \frac{f_j^{(k,l)}}{\sum_i a_{ij}} \sum_{t \in S_l} \frac{a_{itj}}{\sum_{j'} a_{itj'} f_{j'}} \tag{23}$$

$$f_j^{(k+1,0)} = f_j^{(k,L)} \tag{24}$$

where "$f_j^{(k,l+1)}$ is an estimation image at the kth main iteration and lth sub-iteration, S_l is a set of list-mode data in a subset l, L is the number of subsets, j and j' are voxel indexes, a_{ij} is the system matrix indicating the probability that the decay occurring at voxel j is detected at LOR bin i, t is the list-mode event index, and it is the LOR bin of a list-mode event t. For the detector response function (DRF) modeling, we used a Gaussian model in which the weight for each voxel against a LOR is defined as a Gaussian function. The standard deviation of the Gaussian function was set for each LOR to take different crystal sizes for the scatterer and the absorber into account" [12].

In single gamma mode, the WGI system uses the detected energies before and after the scatter to find the Compton cone described in Equation 19 along with the OSEM algorithm used in the PET reconstruction. "The system matrix was defined based on the Compton cone determined with the scatterer-detector position, the absorber-detector position and the cone angle calculated from the scatterer energy [E_1] and the original gamma ray energy information E_0" [12].

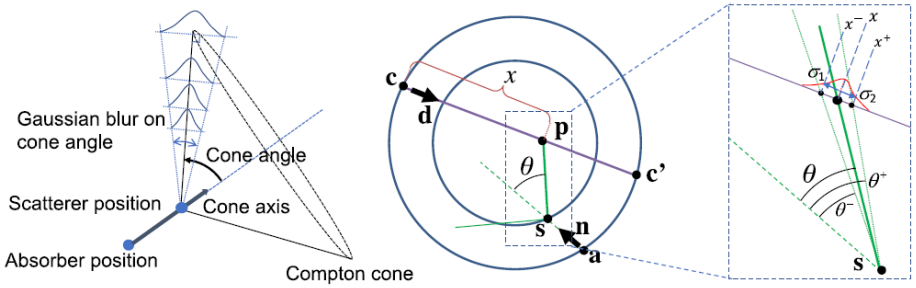

Figure 16: DRF models for (a) the Compton (single gamma) mode reconstruction and (b) the triple gamma mode reconstruction [12]. Note the quantity definitions in (b) and how they relate to the reconstruction equations.

Lastly, in triple gamma mode, the method of back-projection is to reconstruct the image data. The position of the radionuclide can be determined as one of the two intersection points between the Compton cone and the LOR. As shown in Figure 16, the position of the

source is $\mathbf{p}$, and it can be determined using geometry and solving the following system of equations for x:

$$\begin{cases} p & = c + xd \\ \frac{(p-s)n}{|p-s|} & = \cos(\theta). \end{cases} \tag{25}$$

While the system in Equation 25 would be able to determine the source, it does not take into account any factors that would cause blur, namely angle uncertainty due to the energy resolution in addition to the blurring of the LOR. "To convert energy uncertainty to blurring on the LOR, we approximated that the small shift of energy is linearly transferred to that of the location on the LOR. When we let the solution [for x in the system described by Equation 25] be x_0, then, the blurring on the LOR is modeled as an asymmetric Gaussian distribution as follows:

$$h(x) = \begin{cases} \frac{2}{\sqrt{2\pi}(\sigma_1+\sigma_2)} \exp\left(-\frac{(x-x_0)^2}{2\sigma_1^2}\right) & x < x_0 \\ \frac{2}{\sqrt{2\pi}(\sigma_1+\sigma_2)} \exp\left(-\frac{(x-x_0)^2}{2\sigma_2^2}\right) & x \geq x_0 \end{cases} \tag{26}$$

where σ_1 and σ_2 are standard deviations determined by calculating intersection points ... with energies shifted in minus and plus directions, respectively, with the standard deviation of the energy resolution ... Finally, a triple gamma mode image was generated by back-projecting detected events using the proposed DRF incorporating the blurring effects on the LOR with crystal sizes and on the Compton cone with energy resolution" [12].

The WGI prototype was tested with 3 different radionuclides: ^{137}Cs, ^{22}Na, and ^{44}Sc. "The sensitivity and the spatial resolution were measured at the center of the FOV and the 2, 4, 6 and 8 cm off-center positions. Measurement time of the ^{137}Cs point source was 10 min for each position. In the PET mode and the triple gamma mode with ^{22}Na and ^{44}Sc, the measurement time was 120 min for each position. The spatial resolution was measured as the average of radial, tangential and axial FWHMs" [12]. In single gamma mode, the sensitivity and the spatial resolution were 0.22% and 4.4 mm FWHM at the 8 cm off-center position, respectively. In PET mode, the sensitivity and resolution varied with distance, nuclide, and scatterer-scatterer (S-S) vs absorber-absorber (A-A) interactions. Through all testing, the system saw a sensitivity under 2% and a resolution under 2 mm. The S-S interactions had a significantly better sensitivity (under 0.22%) than the A-A interactions, but they both performed about the same in terms of resolution. In triple gamma mode, the average spatial

resolutions for the ^{22}Na and the ^{44}Sc point sources were 4.9 mm and 6.7 mm, respectively. It is worth noting that the triple gamma mode sensitivity was about 1/3000 of the sensitivity in just PET mode.

Although the concept of the Whole Gamma Imaging system had been proven, there was still more progress to be made in terms of making the system medically viable. For starters, in single gamma mode, the team observed a significant variation of spatial resolution over different offsets even for a point source in air which they believed was due to a mismatch between the actual system and the model used in the reconstruction, and they planned to develop a more accurate DRF model. Another problem with the prototype was its awkward size, the diameter of 20 cm of the scatterer is too small for future clinical use and too large for small animal imaging. Problems such as these would be addressed in the future, and the WGI prototype would be used to image more than just point sources of radionuclides.

2.3 Further Developments of WGI

Later in 2020, the same WGI team used their prototype to test 3D reconstruction methods, as well as performing some small animal imaging [13]. The team remodeled the WGI prototype so it could perform small animal imaging and developed an image reconstruction method based on a list-mode ordered subset expectation maximization algorithm incorporating detector response function modeling, random correction, and normalization (sensitivity correction) for either PET or Compton imaging. Rather than reusing the nuclides in Section 2.2, the team chose to use ^{89}Zr as an imaging target, since it emits a 909 keV single-gamma ray as well as a positron when it decays, making it useful for both single gamma and PET imaging modes. Triple gamma mode was not used in these experiments, but they still show how an imaging system with hybrid modalities can be useful in imaging certain isotopes. The team also addressed their concerns from earlier in the year, halving the ring ddiameter so that it could be effectively used for the purposes of small animal imaging.

Since only one radionuclide was being used, the team created an algorithm to determine which imaging mode to use between PET and Compton by the energies of the incoming photons. As seen in the left portion of Figure 17, appropriate energy windows were applied to the energies at the scatterer (E_s) and at the absorber (E_a) do determine what event took place.

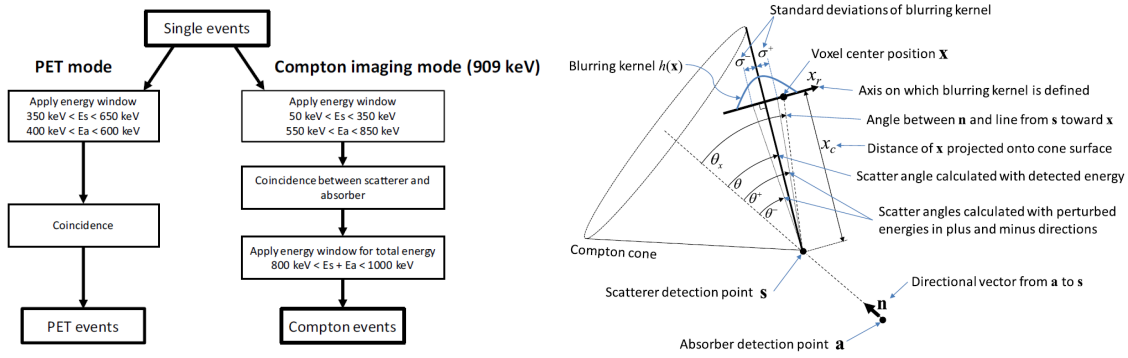

Figure 17: LEFT: Event selection procedure for PET and Compton modes.
RIGHT: DRF model incorporating the angular blurring effect implemented for the Compton imaging [13].

In the case of Compton events, the technique to determine the origin of the event is similar to the one mentioned in Section 2.2, with some added equations and parameters to better account for blur. The quantities associated with the improved DRF can be found in the right portion of Figure 17. One of the changes comes in redefining the gaussian blurring kernel:

$$h_2(x) = \frac{2}{\sqrt{2\pi}(\sigma^+ + \sigma^-)} \exp\left(-\frac{x_r^2}{2\sigma}\right); \sigma = \begin{cases} \sigma^+ & x_r > 0 \\ \sigma^- & \text{else} \end{cases} \tag{27}$$

here called $h_2(x)$ as to not confuse this version with the definition in Equation 26. The DRF of list-mode data consisting of s, a, E_s for the position x is represented with incorporation of distance weights as follows:

$$w(x) = \frac{h_2(x)}{x_c^2 \cdot |s-a|^2}. \tag{28}$$

The image reconstruction algorithm is also similar to the previous iteration, so it will not be further discussed in this paper.

Although cylindrical and small rod phantoms were experimented with and used to measure the sensitivity and resolution of the WGI prototype, the most interesting experiment conducted regarded small animal imaging. "For the small animal experiment, we injected 9.8 MBq ^{89}Zr oxalate into an ICR mouse (male, 5 weeks old, Japan SLC) 23 [hours] before measurement. We conducted a 1 [hour] long measurement, in which the mouse torso was positioned inside the scatterer ring, while the head and tail parts were located outside the scatterer ring as the mouse was longer than the axial length of the scatterer ring ... In

addition, we measured another 1 [hour] only for Compton imaging by placing the upper half of the mouse body inside the scatterer ring to compare characteristics of Compton imaging inside and outside the scatterer ring. The radioactivity distributions in Compton images were compared with a PET image, and noise in images were visually evaluated" [13].

The reconstruction of the PET and Compton images of the mouse are shown in Figure 18. The mouse was longer axially than the scattering ring for Compton mode but almost the entire body was imaged. Although at first glance the PET and Compton images seem comparable, there are differences in image quality within and outside the scattering ring for the Compton image. Inside the ring, the Compton region mostly agreed with the PET image, however high accumulation on the top of the head located in the outside region, which was not observed in the PET image. Also, the eye cavities in the skull were easily identifiable in the PET image, but not with the Compton image. "Although the image quality was not as good as the PET image, the WGI Compton imaging could provide highly accurate measurements for the region inside the scatterer ring" [13]. The energy resolution of the scatterer detector of the WGI prototype was 17% at 511 keV, which was not as good as typical Compton imaging systems, but they were able to achieve a spatial resolution of less than 3 mm.

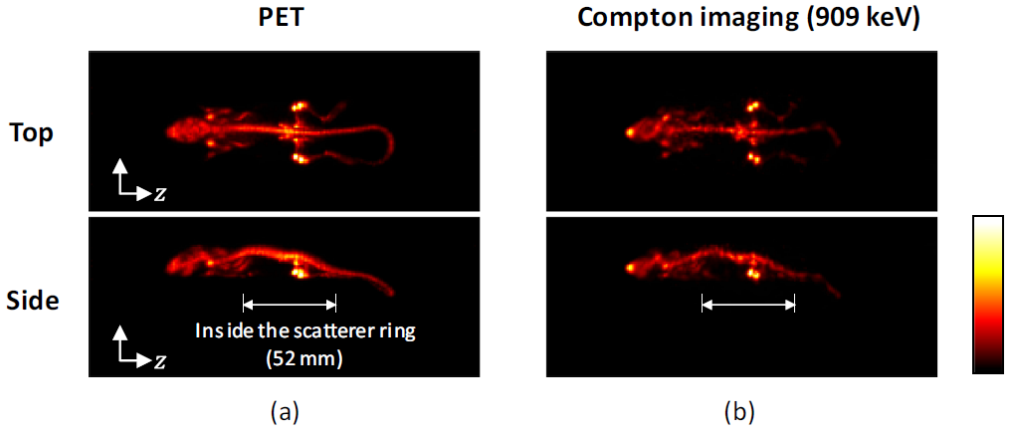

Figure 18: Reconstructions of the mouse injected with ^{89}Zr [13]. Column (a) shows the PET reconstruction and column (b) shows the Compton reconstruction. The upper row shows the maximum intensity projection (MIP) images from the top and the lower row shows those from the side.

The team identified four points of success in achieving the quality of Compton imaging approach that of PET. Firstly, the choice of the ^{89}Zr isotope produced a high-energy (909 keV) gamma ray which led to sharper images and better resolutions. Isotopes that decay

into a positron as well as high-energy gamma rays are preferable since they can be used in hybrid systems such as the WGI prototype. Secondly, the team's DRF model for image reconstruction assuming the blurring effect depends only on energy uncertainty approximated the actual system with sufficient accuracy. Thirdly, the team's use of normalization was essential to maintain uniformity in images, using their method to calculate the global sensitivity image directly from the list-mode data measured for normalization. Lastly, the full-ring geometry enabled enough sampling of projection view angles as well as increasing the number of counts. The WGI prototype was the first of its kind to include triple gamma imaging and proved to be a step in the right direction for hybrid imaging systems. It would inspire similar systems that would try and simultaneously image using PET and Compton methods.

2.4 In-Vivo Imaging with a Compton-PET Hybrid Camera

In 2021, part of the team that helped developed the WGI prototype created a Compton-PET hybrid camera (CPHC) for the purposes of imaging radionuclide tracers in the bodies of mice and seeing how they target cancerous tumors [14]. One of the main goals of this camera system is to reconcile PET and SPECT methods without the need for a collimator, which allows for nuclides that decay into different energies to be used and imaged. The more imaging methods are used in treatment, the more accurate the diagnosis. A diagram of the CPHC system is shown in Figure 19, and the influence from the WGI prototype can be seen.

"The detector configuration of the prototype Compton-PET hybrid camera comprises two modules of scatterers and absorbers, each containing pixelated scintillator arrays and silicon photomultipliers (SiPMs). To visualize a SPECT tracer using Compton imaging requires suitable energy resolution. Therefore, we chose a high-resolution-type Ce:$Gd_3Al_2Ga_3O_{12}$ (HR-GAGG) scintillator for this study. A GAGG scintillator has the characteristics of desirable energy resolution (4% with an avalanche photodiode [APD]), high light yield (56,000 photons/MeV), high density (6.63 g/cm3), moderate decay time (150 ns), non-deliquescence, and non-selfirradiation. The scattering layer was an 8 × 8 HR-GAGG array of 2.5 mm × 2.5 mm × 1.5 mm scintillators that was used to detect Compton scattering of low-energy gamma rays from SPECT nuclides, and the absorbing layer was an 8 × 8 HR-GAGG array of 2.5 mm × 2.5 mm × 9 mm scintillators that was used to detect photon absorption of the

511 keV gamma rays from the PET nuclides. The scatterer thickness was decided so that a Compton scattering possibility would be more than 15% for an energy of 150 keV and less than 10% for an energy of 511 keV. The pitch size was 3.2 mm, and each crystal was separated by BaSO4 reflectors. Each GAGG array was coupled to an 8 × 8 array of SiPMs (Hamamatsu MPPC S13361-3050) and was then wrapped with Teflon tape" [14].

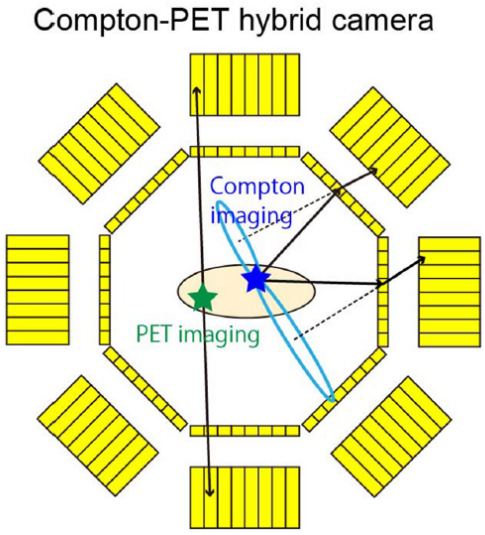

Figure 19: Diagram of the Compton-PET Hybrid camera [14]. Notice the similarities between this and the WGI prototype.

The CPHC simultaneously imaged both ^{18}F-FDG, a PET nuclide as well as ^{111}In, a SPECT nuclide utilizing microtubes as well as in-vivo within mouse specimens. ^{18}F-FDG is a positron emitter, which yields a pair of annihilation gamma rays with an energy of 511 keV and ^{111}In emits gamma rays with energies of 171 keV and 245 keV. The tracers were injected into a male nude mouse bearing an SY tumor, a small-cell lung cancer cell line, then subsequently imaged using the CPHC. Images of the mice are shown in Figure 18, and it can be seen how ^{111}In was able to target the tumor better than ^{18}F. Different organs became more or less visible in the image depending on the tracer and imaging method used. Systems such as the CPHC allow for simultaneous imaging using multiple methods, which gives more information allowing for a more accurate diagnosis.

The spatial resolution of the CPHC was not as good as that of commercial small-animal PET scanners, however it was not optimized for strictly PET imaging. In PET mode, the spatial resolution was 3.3 mm, and in Compton mode, the spatial resolution was 4.2 mm. "There is room to improve the spatial resolution in terms of the detector pixel size—which

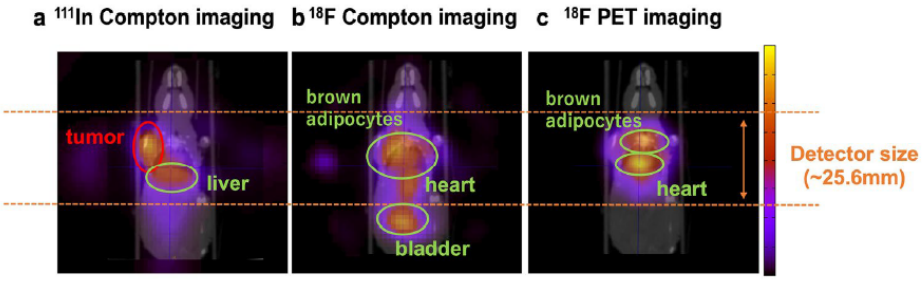

Figure 20: Images of the nuclides injected into a mouse specimen superimposed over the CT image [14]. (a) shows the Compton image of the mouse using the ^{111}In nuclide, (b) shows the Compton image of the mouse using the ^{18}F-FDG nuclide, and (c) shows the PET image of the mouse using the ^{18}F-FDG nuclide. Select organs as well as the tumor are strongly visualized.

mostly determines the spatial resolution—the time resolution, and the method of reconstruction ... We are going to build a ring Compton-PET hybrid camera as the second prototype imaging system. Moreover, PET imaging is a well-established method, and the spatial resolution has been improved by using information about the depth of interaction (DOI) and the time-of-flight (TOF). These techniques also can be applied to our Compton-PET hybrid camera to improve the spatial and the time resolution." [14]. Something else that could be improved in the future is dealing with multiple scatterings within a body before a photon reaches the detector. In larger animals and humans, in-vivo tracers have a larger chance of scattering within the body, losing energy and making image reconstruction and tracer location more difficult. "Recently, we demonstrated the scatter correction method in the Compton imaging system by setting arbitrary scattering points on the attenuating material. As the method to reduce crosstalk artifacts, a dual-energy-window scatter correction, which is used in SPECT imaging, for multi-nuclide Compton imaging ... By using these techniques, the scattered photons and crosstalk events could be reduced, resulting in the improvement of Compton images" [14].

2.5 Coded Aperture and Targeted Alpha-Particle Therapy

One of the most interesting and robust papers recently published on the topic of using Compton methods to image nuclides involved in Targeted Alpha-Particle Therapy (TAT) comes from a team in California, mainly interested in ^{225}Ac and its daughter emissions [15]. The team was particularly interested in ^{225}Ac because it has promise in targeting and treating cancerous tumors. It has a relatively long-lived radiometal with a half-life $t_{1/2}$ of 10 days

and its decay pathway yields four alpha particles with contributions from the daughters ^{221}Fr ($t_{1/2} = 4.90$ min), ^{213}Bi ($t_{1/2} = 45.6$ min), and ^{213}Po ($t_{1/2} = 4.2$ μs). Since the decay of ^{225}Ac or its daughters do not include any positrons, it is impossible to image using PET methods. The daughters decay into 218 keV and 440 keV gamma rays, which makes it awkward to image using SPECT methods as gamma ray energies above 300 keV have a degradation of response since there is a higher likelihood of photon transmission through the collimator, and energies below 300 keV result in lower-quality sensitivities. If only one of these properties were present, they could be compensated for; however, since both are present it is difficult to implement SPECT methods while optimizing tradeoffs. These issues have caused the implementation and research surrounding the usage of ^{225}Ac in TAT to be slowed.

Through the use of combining coded apertures with Compton imaging methods together, the daughter distributions can be better imaged compared to PET and SPECT methods. For photon energies under a few hundred keV, coded apertures are advantageous since they can decouple the dependence of resolution on sensitivity, providing the maximum possible sensitivity among collimator-based systems. As described in Section 1.4 coded apertures increase photon acceptance by opening many small pinholes as opposed to widening a single one. The shape of the mask is chosen to optimize photon acceptance as well as resolution. Coded apertures help the issue of imaging the 218 keV decay, but they still have the same problem of having quality degradation at higher energies. At higher energies, Compton imaging methods yield more fruitful results. As previously discussed, the resolution of the Compton image is tied to the energy of the incident photon, so a dual-modality imager with both coded aperture and Compton methods would allow for better imaging of decaying ^{225}Ac nuclides. The system is shown in Figure 21, and the rough geometry of the aperture mask can be seen. "The coded aperture is fabricated from 2:4-mm-thick tungsten, which ensures roughly 90% attenuation at 250 keV. The mask consists of 64 by 64 square elements with each individual element having a 2 by 2 mm^2 face to match the detector pixel size and limit collimation effects. This equates to a total mask area that is about four times larger than that of the detector. The elements are arranged in a random pattern with a 50% open fraction. The pattern was optimized across a range of magnifications using a combinatorial search technique" [15].

Similar to the WGI prototype and the CPHC, the dual-modality TAT imager uses Equa-

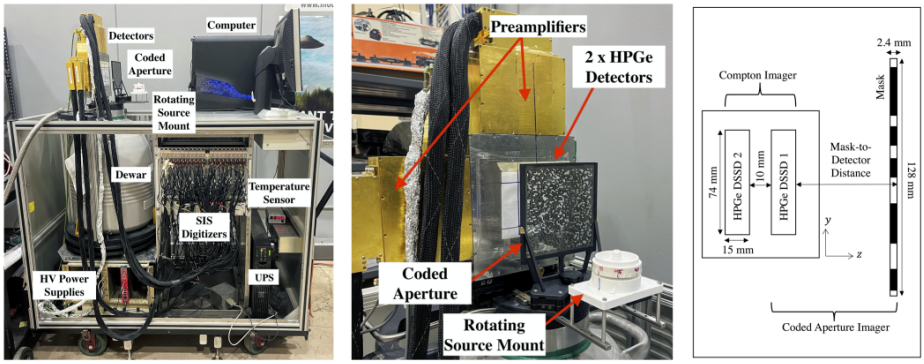

(a) (b) (c)

Figure 21: Dual-modality imager with Compton and coded aperture capabilities [15]. (a) shows the system in its entirety, while (b) shows a closeup of the detector/mask arrangement. (c) is a schematic drawing of the Compton and coded aperture geometries.

tion 19 to measure the energy of the scattered photon to find the Compton cone. However, unlike those systems, instead of using PET or SPECT methods to find a simultaneous LOR, this system images the nuclide by acquiring many Compton events and analyzing the intersection of the associated cones, back-projecting them and using the information to determine the gamma ray distribution. In terms of resolution, the detectors exhibit favorable energy resolution, on average between 0.2% and 0.5% at 662 keV, due to the detection properties of HPGe. The spatial resolution of the coded aperture imager came out to be approximately 6.9 mm at full-width half-maximum (FWHM) while the spatial resolution of the Compton imager was approximately 4.1 mm at FWHM. These resolutions were verified by imaging ^{57}Co and ^{137}Cs discs, respectively. Unlike the WGI and CPHC, this system is not a simultaneous imager, rather it is capable of imaging in two modes separately.

The system's capabilities of measuring the decay of ^{225}Ac were tested both using phantoms as well as in-vivo. For the phantom experiment, three spheres of different diameters (4.6 mm, 6.6 mm, and 8.3 mm) were filled with ^{225}Ac, submerged in a cylinder of water, and placed in a triangular configuration. The phantom was first imaged in coded aperture mode 2 days after preparation. The phantom was placed in front of the coded aperture detector and imaged in 30-minute increments, rotating 45° after every increment. The total imaging time was 4 hours. The phantom was also imaged in Compton mode 12 days after preparation and underwent the same process as it did in coded aperture mode. The experimental setup of the microspheres and each imaging mode is shown in Figure 22.

The results of the phantom testing had the coded aperture mode reconstruct spheres

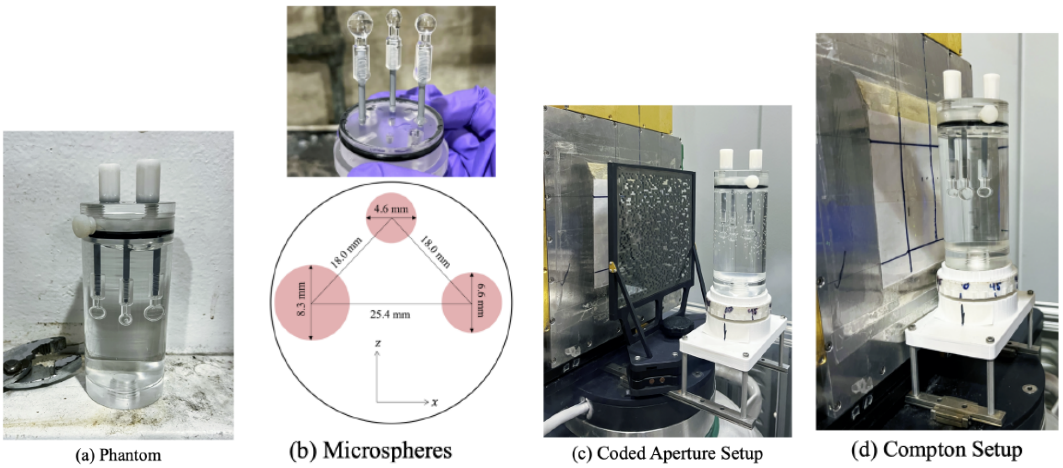

(a) Phantom (b) Microspheres (c) Coded Aperture Setup (d) Compton Setup

Figure 22: Setup and geometry of imaging the phantom [15]. (a) Shows the three microspheres of ^{225}Ac submerged in a cylinder of water, (b) shows the geometry of the microspheres, and (c) and (d) show the imaging setups for the coded aperture and Compton modes, respectively.

at the central linear cross-section are 7.2 mm, 7.9 mm, and 8.1 mm in FWHM in order of the smallest to largest sphere, respectively. The Compton mode reconstructed spheres at the central linear cross-section are 6.8 mm, 7.6 mm, and 7.9 mm in FWHM in order of the smallest to largest sphere, respectively. It is obvious that the reconstructed sizes are not the same as the actual geometry of the microspheres, and the main cause of this discrepancy is the subpar spatial resolution. However, the system was able to accurately determine the activity of each microsphere, within 2 Bq of the actual value in both coded aperture and Compton modes [15].

As mentioned above, the system was also used to measure ^{225}Ac in-vivo. "Five- to six-week-old male athymic mice were implanted subcutaneously with prostate cancer cells into the right flank ... Approximately 3 to 5 weeks after tumor implantation, the mice were injected with [^{225}Ac tracers] via the tail vein and sacrificed at different time intervals to evaluate the tumor-targeting specificity" [15]. Two mice were imaged, Mouse A 2 days after injection of its ^{225}Ac tracer and Mouse B 4 days after injection of its ^{225}Ac tracer. The mice received different flavors of tracers, ^{225}Ac-Macropa-PEG8(7)-YS5 and ^{225}Ac-DOTA-YS5, respectively. The mice were imaged using both methods and were housed in a 50 mL falcon tube and stored in a freezer at 20°F when not in use. The imaging setup can be seen in Figure 23. Since the team saw extremely similar results between the two mice, this paper will only discuss the imaging and results of Mouse A.

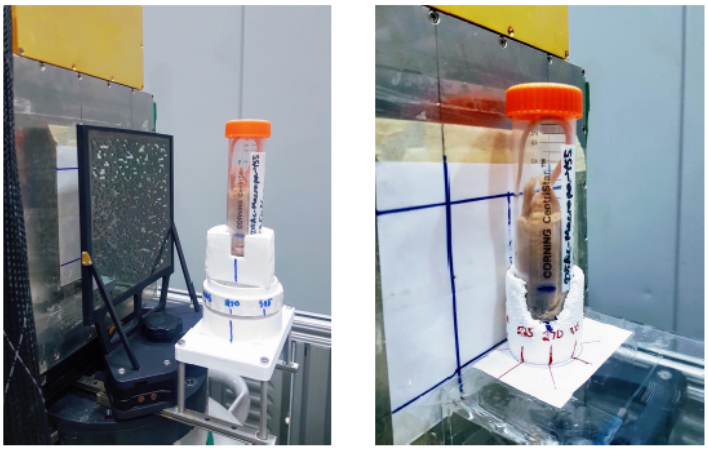

(a) Coded Aperture Setup (b) Compton Setup

Figure 23: Experimental setup showing the imaging of a mouse in (a) Coded=aperture mode and (b) Compton mode [15].

Similar to the phantom, Mouse A was imaged in both coded aperture and Compton mode. However, in coded aperture mode, the mouse was rotated 45° in increments of 60 minutes, with a total imaging time of 8 hours. In Compton mode, it was rotated in increments of 75 minutes, with a total imaging time of 10 hours. Mouse A was also imaged using CT separately, and the coded aperture and Compton reconstructions overlayed over the coronal slice of the CT image can be seen in Figure 24. The images were able to show the location of the induced tumor, as well as showing the ^{225} tracer targeting it.

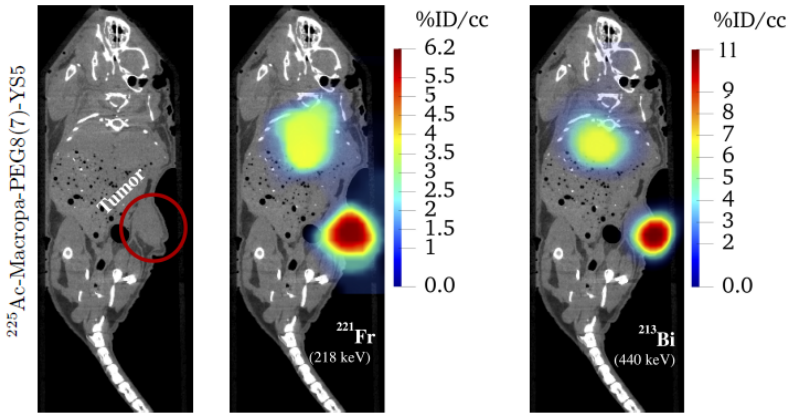

(a) 2-D CT (b) 2-D CT + Coded Aperture (c) 2-D CT + Compton

Figure 24: Images of Mouse A [15]. (a) is just the CT image of the coronial slice, (b) overlays the coded aperture image on top of it while (c) overlays the Compton image. Notice how in (b) and (c) the images show the nuclide heavily targeting the tumor, as well as showing up in the central organs.

After imaging, an autopsy was performed on the mouse in order to measure the activity

of the organs and tumor and compare them to the results from using the imaging system. The liver, heart, kidney, lungs, spleen, pancreas, muscle, bone, and subcutaneous tumor were harvested, weighed, and counted by a Hidex Automated Gamma Counter. The system did a good job of determining the activity of the tumor, within about 5.8% error in coded aperture mode and about 2.7% error in Compton mode. However, due to the limited spatial resolution or gravitational effects creating an amalgamation of organs, the system was unable to distinguish between and thus determine the activity of the individual central organs. When compared to the "sum" of the activity of the central organs performed ex-vivo, the system was within about 7.5% error in the coded aperture mode and within about 7% error in Compton mode [15]. The dual-modality imaging system has demonstrated feasibility in imaging the daughters of ^{225}Ac using both coded aperture and Compton methods.

3 Discussion and Conclusion

Although the Compton and hybrid imaging methods described throughout Section 2 are exciting and show promise as emerging medical imaging technologies, it is important to note that the field is still relatively young and there will still be trials and tribulations before any of the techniques become ready for commercial use on animals or humans. The WGI prototype already went through changes to be able to be used in in-vivo experiments, and it still took extremely long to image a dead mouse. Same with the dual-modality imager used for TAT. In the field, it is not reasonable to expect a live human or animal will stay still for 8+ hours to be constantly imaged. The timing of these imaging experiments must be made faster without sacrificing image quality before they are ever brought to market. Something else that will most likely see improvement before systems like these move on from prototypes will be the image reconstruction algorithms. The reconstruction algorithms used by each project were clever in the way they took the basic Compton scatter equation and use detected energy measurements to determine the position of activity. Methods such as back-projection, MLEM, and DRF have been implemented and improved between projects, and they will continue to improve as the systems get closer to commercial viability.

One of the more egregious issues with systems such as these is the relatively poor spatial resolution. As mentioned earlier CT is an extremely popular imaging technique due to its favorable resolution but have issues when it comes to differentiating anomalies from healthy

but abnormal tissue. Compton and hybrid imaging techniques, combined with TAT, prove successful at determining if a cancer is present within a body and the general location of where it may be, but the poor resolution leaves much to be desired. In Section 2.5, the induced tumor was nowhere near the central organs in the mouse, and the imaging system was able to pick up on its general location within the body. However, if the tumor were much smaller, or on or near a central organ, the system would have a difficult time determining its location. Coded aperture masks and choice materials and geometries for scatterer-absorbers can help mediate the problem, along with improvements in high-energy detector technologies and measurement techniques.

This paper has discussed a few select methods utilizing Compton and hybrid imaging techniques for medical purposes. Though a relatively new development in the medical field, it has nevertheless made strides over the past 2 decades. With the advancements in geometry, reconstruction algorithms, and chemical sciences, some of the systems mentioned have a good chance of evolving and eventually being used commercially for the purposes of small-animal and human imaging. It is unlikely that Compton and hybrid imaging systems will replace the methods in the near future. They are exciting and promising developments and will surely supplement the available technologies, leading to better data collection and more accurate diagnoses.

References

[1] S. J. Ling *et al.*, *University Physics Volume 3*. OpenStax, 2016. [Online]. Available: https://openstax.org/details/books/university-physics-volume-3

[2] S. J. Norton, "Compton scattering tomography," *Journal of Applied Physics*, vol. 76, no. 4, pp. 2007–2015, 1994.

[3] R. Devanathan, L. Corrales, F. Gao, and W. Weber, "Signal variance in gamma-ray detectors—a review," *Nuclear Instruments and Methods in Physics Research A*, pp. 637–649, 2006.

[4] J. S. Lewis, S. Achilefub, J. Garbow, R. Laforest, and M. Welch, "Small animal imaging: current technology and perspectives for oncological imaging," *European Journal of Cancer*, vol. 38, p. 2173–2188, 2002.

[5] R. Harrison, M. Kaplan, S. Vannoy, and T. Lewellen, "Positron range and coincidence non-collinearity in simset," 1999.

[6] R. Hadfield, "Single-photon detectors for optical quantum information applications," *Nature Photonics*, vol. 3, pp. 696–705, 2009.

[7] A. Farber and J. Williams, "Coded-aperture compton camera for gamma-ray imaging," *EPJ Web of Conferences*, pp. 1–9, 2016.

[8] C. Grignona *et al.*, "Nuclear medical imaging using $\beta^+\gamma$ coincidences from ^{44}sc radionuclide with liquid xenon as detection medium," *Nuclear Instruments and Methods in Physics Research*, no. 571, pp. 142–145, 2007.

[9] L. Gallego Manzano *et al.*, "Xemis: A liquid xenon detector for medical imaging," *Nuclear Instruments and Methods in Physics Research A*, vol. 787, pp. 89–93, 2014.

[10] ——, "Xemis2: A liquid xenon detector for small animal medical imaging," *Nuclear Instruments and Methods in Physics Research A*, vol. 912, pp. 329–332, 2018.

[11] H. Tashima and T. Yamaya1, "Compton imaging for medical applications," *Radiological Physics and Technology*, vol. 15, pp. 187–205, 2022.

[12] E. Yoshida, H. Tashima, K. Nagatsu, A. B. Tsuji, K. Kamada, K. Parodi, and T. Yamaya, "Whole gamma imaging: a new concept of pet combined with compton imaging," *Physics in Medicine and Biology*, vol. 65, pp. 1–14, 2020.

[13] H. Tashima, E. Yoshida, H. Wakizaka, M. Takahashi, K. Nagatsu, A. B. Tsuji, K. Kamada, K. Parodi, and T. Yamaya, "3d compton image reconstruction method for whole gamma imaging," *Institute of Physics and Engineering in Medicine*, vol. 65, no. 225038, pp. 1–15, 2020.

[14] M. Uenomachi, M. Takahashi, K. Shimazoe, H. Takahashi, K. Kamada, T. Orita, K. Ogane, and A. B. Tsuji, "Simultaneous in vivo imaging with pet and spect tracers using a compton-pet hybrid camera," *Nature Portfolio*, vol. 11, pp. 1–11, 2021.

[15] E. A. Frame, K. N. Bobba, D. L. Gunter, L. Mihailescu, A. P. Bidkar, R. R. Flavell, and K. Vetter, "Coded aperture and compton imaging for the development

of targeted alpha-particle therapy," *The Computer Journal*, 2022. [Online]. Available: https://arxiv.org/abs/2212.07631